AIAA JOURNAL
Vol. 48, No. 10, October 2010

Large Eddy Simulation of Stable Supersonic Jet Impinging on Flat Plate

A. Dauptain,* B. Cuenot,† and L. Y. M. Gicquel‡
Centre Européen de Recherche et Formation Avancée en Calcul Scientifique, 31057 Toulouse, France

DOI: 10.2514/1.J050362

This paper describes a numerical study based on large eddy simulation of the flow induced by a supersonic jet impinging on a flat plate in a stable regime. This flow involves very high velocities, shocks, and intense shear layers. Performing large eddy simulation on such flows remains a challenge because of the shock discontinuities. Here, large eddy simulation is performed with an explicit third-order compressible solver using a unstructured mesh, a centered scheme, and the Smagorinsky model. Three levels of mesh refinement (from 7 to 22 million cells) are compared in terms of instantaneous and averaged flowfields (shock and recirculation zone positions), averaged flow velocity and pressure fields, wall pressure, root mean square pressure fields, and spectral content using one and two-point analyses. The effects of numerical dissipation and turbulent viscosity are compared on the three grids and shown to be well controlled. The comparison of large eddy simulation with experimental data shows that the finest grid (a 22 million cell mesh) ensures grid-independent results not only for the mean and rms fields but also for higher statistics such as single and two-point correlation functions.

Nomenclature

C_p	=	heat capacity at constant pressure, J.Kg^{-1}.K^{-1}
c	=	sound speed, m/s
d	=	nozzle inner diameter, 2.54 cm
h	=	wall-nozzle distance, 10.5664 cm
p	=	pressure, Pa
q	=	heat flux, J.m^{-2}.s^{-1}
R	=	ideal gas constant, 8.314 J.K^{-1}.mol^{-1}
r	=	cylindrical coordinate : distance from the axis, m
S_{ij}	=	strain rate tensor, s^{-1}
T	=	temperature, K
t	=	time, s
u, v, w	=	velocity components, m/s
V	=	cell volume, m^3
W	=	molar mass of air, 28.85 g.mol^{-1}
$\mathbf{x}$, x, y, z	=	Cartesian coordinates: vector and components, m
Δx	=	cell size and implicit filter width, m
Δt	=	computational time step, s
Δ_{Cell}	=	size of compression-expansion zone, m
μ	=	dynamic viscosity, Kg.m^{-1}.s^{-1}
ρ	=	density, Kg/m^3
τ_{ij}	=	stress tensor, Kg.m.s^{-2}
Φ	=	phase shift, rad
$\bar{}$	=	spatial filtering of large eddy simulation
$\sim$	=	Favre averaging
$\hat{}$	=	Fourier transform
$\langle\rangle_{\text{mean}}$	=	mean, in the process of time-averaging
$\langle\rangle_{\text{rms}}$	=	root mean square or quadratic mean, in the process of time-averaging
$\langle\rangle_{\text{az.}}$	=	azimuthal averaging

Received 7 December 2009; revision received 18 June 2010; accepted for publication 7 July 2010.

*Senior Searcher, CFD team, 42 Ave. G. Coriolis; dauptain@cerfacs.fr.
†Senior Searcher, CFD team, 42 Ave. G. Coriolis; cuenot@cerfacs.fr.
‡Senior Searcher, CFD team, 42 Ave. G. Coriolis; lgicquel@cerfacs.fr.

I. Introduction

IN RECENT years, large eddy simulations (LES) have demonstrated their ability to predict the behavior of weakly compressible turbulent flows [1–5]. LES applications to supersonic flows, however, remain to be validated. Typical examples of non-reacting supersonic flows with strong industrial interests are impinging jets which appear in leaks of high-pressure tanks and pipes or breaches in the outer structure of reentry vehicles [6]. Such jets can exhibit tone-producing modes that depend on the jet exit distance to the wall and nozzle pressure ratio [7–9]. They have been studied for astronautics (multistage rocket separation, attitude control thruster), aeronautics (jet-engine exhaust impingment. vertical takeoff stability) or turbomachinery (gas turbine blade thermal failure). The 1971 work of Donaldson and Snedeker [10] and Donaldson et al. [11] describes the physics of circular jets impinging on spherical, normal and oblique surface. A later work from Lamont and Hunt [12] focuses on the near field jet impingement zone, showing the link between the overall load on the plate and the momentum flux at the nozzle lip. A fair amount of studies focused in the eighties and nineties on the unsteadiness of such flows, e.g., Ho and Nosseir [13], Kuo and Dowling [14].

Computational approaches based on the method of characteristics or Euler solvers are common tools for supersonic jets. Reynolds Averaged Navier–Stokes (RANS) simulations address the viscous features and the effect of turbulence. These numerical models are widely developed and computationally efficient but they are limited to stationary flows. Unsteady phenomena linked to turbulence are best addressed with LES, which provides time-dependent filtered quantities of one flow realization. LES has been used with success to reproduce the intermittent and unsteady tone-producing modes of freejets [15] and cavities [16]. Combined with advanced diagnostics to take advantage of the spatial and temporal description of the problem, LES can provide specific informations about nonlinear interactions or causality of phenomena.

From a chronological point of view, specific numerical techniques have been developed for supersonic jets since the fifties. The work of Ferri at NACA [17] illustrates the sophistication of the characteristics approach in the context of transonic aircrafts. The BAMIRAC report of Adamson [18] reviews several approximate methods to calculate the main inviscid features of highly underexpanded jets. Between 1990 and 2000, various Euler or RANS solvers took advantage of adaptive gridding or multigrid [19–23]. Oscillating impinging jets were simulated by Kuo and Dowling [14] and Sakakibara and Iwamoto [24]. Improvements of turbulence models lead to accurate

Table 1 Selection of previous numerical works

Case	Name	Year	Method	Mesh	Volume	Size (DOF)
Imp. jet	Arunajatesan [27]	2002	LES	Structured	30° sector	$5 \times 2.78 \times 10^6$
Mix. lay.	Georgiadis [36]	2003	Hybrid	Structured	3D slab.	$5 \times 0.87 \times 10^6$
Freejet	Cheng [37]	2005	ILES-WENO	Structured	2D Axisym.	$4 \times 87.5 \times 10^3$
Screech. Jet	Berland [15]	2006	LES	Structured	3D slab	$5 \times 16.3 \times 10^6$
Ctrld. Jet [a]	Chauvet [38,39]	2007	RANS and Hybrid	Structured	3D	$5 \times 10.5 \times 10^6$
Screech. Jet	Singh [40]	2007	LES-WENO	Structured	2D Axisym.	$4 \times 210 \times 10^3$
Launcher Nozzle	Deck [41]	2009	Hybrid	Structured	3D	$5 \times 11 \times 10^6$
Imp. Jet	Present work	——	LES	Unstructured	3D	$5 \times 3.8 \times 10^6$

[a]Complex geometry with mixing enhancement by control jets.

quantitative predictions [25], and unsteady RANS succeded in reproducing screech phenomenon [26], in spite of a narrow bandwith description around the discrete tone. In 2003, Arunajatesan and Sinha [27] used LES for steady supersonic impingement of jets, to predict the major quantities of the flow such as the averaged pressure loads and centerline velocity. A few studies focused also on planar [28] and rectangular [29] supersonic screech jets. Note that direct computation of noise by LES has been also demonstrated in subsonic configurations [30–32]. More recently, hybrid methods mixing RANS and LES approaches were applied successfully to compressible mixing layers [33] and to supersonic jets [34], to address the problem of wall-generated turbulence, a recurrent LES bottleneck [35]. Note that wall-generated turbulence in the nozzle of a freejet does have a clear impact on the noise generated and special care must be taken (e.g., [15]) for stable regimes, but it is not first-order in the loud discrete tones of unstable impinging jets.

Table 1 presents a selection of numerical works in the last decade related to similar configurations, considering the studies of Arunajatesan and Sinha [27], Berland et al. [28], Georgiadis et al [36], Cheng and Lee [37], Chauvet et al. [38,39], Singh and Chatterjee [40], and Deck [41]. The degrees of freedom are the total number of unknowns. WENO approaches having a high CPU cost, the simulation domain and related grids are significantly smaller. Structured grids are mainly used because the academic impingement configuration is geometrically simple. On the other hand, unstructured grids are attractive for the short human time spent in the gridding phase, the freedom of refinement/coarsening in any direction, and its ability to deal with complex geometries.

The scope of this work is to establish what are the numerical cost and constraints of LES to adequately study supersonic impinging jets. It is also of interest to know if the convergence of simulations can be achieved with an acceptable cost, and if so does the dataset supply satisfactory second-order diagnostics: two-point correlations without potential bias from the mesh resolution for example. To do so, the present study includes a discussion on mean grid convergence and the quantification of specific LES parameters. Note that the conclusions obtained here are restrained to LES of a supersonic jet impinging on a wall using a centered scheme with hyperviscosity at shocks and unstructured grids. These may differ if a different strategy is adopted.

The paper is organized as follows. The experimental target configuration is introduced in Sec. II, with a brief flow description. Then, the numerical method is presented and commented with particular stress on shock-capturing technique and high performance computing (Sec. III). The analysis is focused on the validation of time-averaged quantities with respect to experimental data, the observation of several flow features referenced in the literature, and the energy distribution through spectral analysis. A specific attention is devoted to the influence of the mesh on the LES solution. This study concludes with a discussion on the pros and cons of LES applied to such flows.

II. Target Configuration

Standing at the intersection of screech investigation and impinging jets, the experimental work of Henderson et al. [7] is of particular interest to LES. Indeed, the variation of a single geometric parameter, namely the nozzle to plate distance, leads either to silent or tone-producing flows. The current work aims at assessing the validity of LES on one of the stable cases.

A. Flow Description and Parameterization

The flow parameters governing the response of free supersonic jets are: the convergent nozzle of diameter d and the nozzle total pressure to ambient static pressure ratio (NPR). For a NPR approaching four,

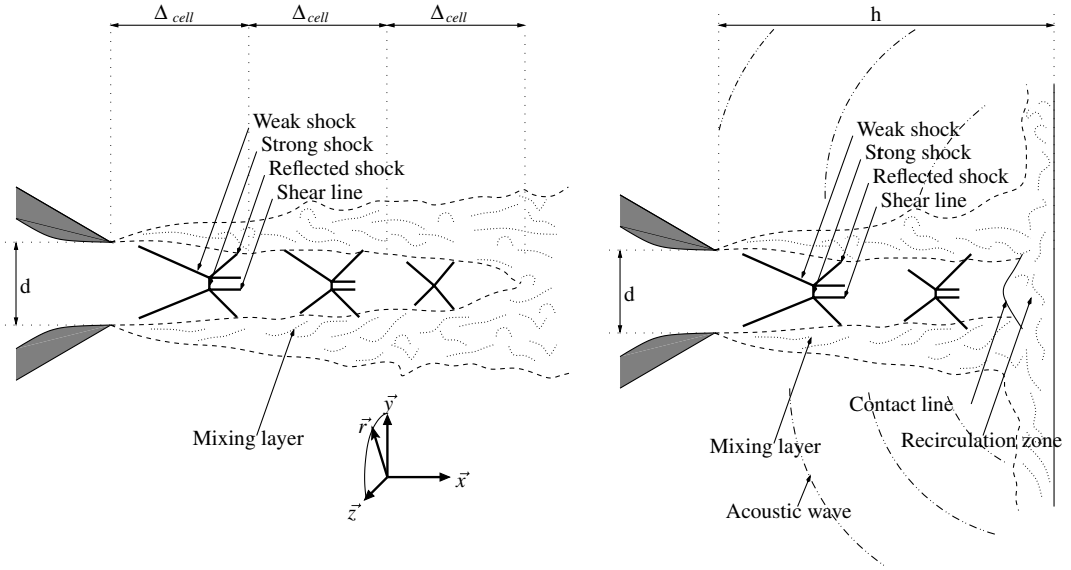

a) Free jet **b) Impinging jet**

Fig. 1 Impacting jet on a flat plate: flow description and main geometrical parameters.

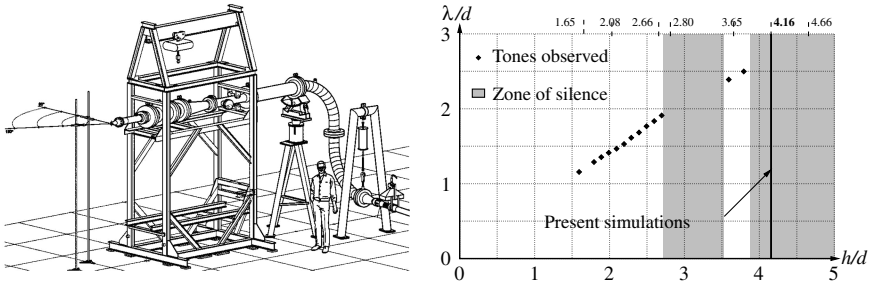

Fig. 2 Small hot-jet aeroacoustic rig, facility of the aeroacoustic propulsion laboratory, NASA Glenn Research Center: a) view of the laboratory setup, and b) the different regimes observed experimentally.

shock structures take place at the rim of the nozzle. The fluid goes through a Prandtl–Meyer expansion to recover the ambient pressure value. Mach reflections converge to generate a cone-shaped weak shock ended by a disc-shaped strong shock, Fig. 1a. The weak and strong shocks merge into a triple point giving birth to a reflected oblique shock and a shear line. For freejets, this inviscid pattern composed of the weak, strong, reflected shocks and shear lines is repeated several times downstream. The size of this expansion-compression cell Δ_{cell} was measured for a wide range of configuration [42]. The succession of cells is the primary mechanism by which the jet inner pressure adapts to reach the ambient state.

For impinging configurations, a large obstacle (usually a wall, Fig. 1b) is blocking the supersonic freejet plume. The most critical configuration appears if the distance h from the jet nozzle to the wall is shorter than the inviscid core. For that case, the strong pressure drop issued by the strong shock creates a near wall flow recirculation bubble with a contact line separating the main jet and the recirculated flow as shown on Fig. 1b. The main effect of this impact of the jet on the wall is the generation of strong acoustic waves and depending on the NPR, the wall distance h/d or the plate dimension, discrete acoustic tones may be produced.

Although the extreme case of the tone dominated impacting jet is of clear interest, a simpler stable case is retained for this study which aims at producing a detailed LES validation. For this reason the present work focuses on the stable case studied experimentally by Henderson et al. [7] and defined by NPR $= 4.03$, $h/d = 4.16$.

B. Experimental Apparatus and Diagnostics

The experiment performed by Henderson et al. [7] uses the Small Hot Jet Aeroacoustic rig, a facility of the AeroAcoustic Propulsion Laboratory at the NASA Glenn Research Center, Fig. 2a. In this specific experiment, the convergent nozzle has a 1 in. exit diameter d, with an external contour of a 30 deg cone, and discharges into ambient air. The NPR equals 4.03 for a jet temperature close to 300 K. The outflowing gas is air seeded with olive oil droplets to allow measurements by digital particle imaging velocimetry (DPIV). Microphone recordings are also available away from the impact, in a region affected by acoustics only.

An aluminum plate orthogonal to the jet axis is mounted in front of the nozzle at a distance h that can be moved from $h/d = 1.5$ to 5. By varying the axial distance h/d, the experimental layout allows different tone-producing regimes, with a fundamental frequency amplitude often 20 dB above the broadband noise. In particular, symmetrical jet oscillations occur for $h/d < 2.7$, a zone of silence appears for $2.7 < h/d < 3.5$ and tone-producing regimes are observed again for $3.5 < h/d < 3.8$. There is no more tone-producing regimes in the interval $3,8 < h/d < 5$ (Fig. 2b). The condition studied here corresponds to $h/d = 4.16$.

III. Numerical Approach

A. Computational Domain and Boundary Conditions

To avoid difficulties associated to boundary conditions, the simulation is set up with a numerical blowdown configuration in which a very large tank feeds another large tank trough a supersonic impinging jet. This allows to use walls on all boundaries (Fig. 3). The sizes of the tanks are taken large enough to make the simulation time negligible with respect to the overall discharge time.

Quantitatively, the tank radii are of the order $500 \times d$, leading to approximately $m_i = 1000$ kg of mass enclosed initially in the high-pressure tank. The mass flow rate at the operating condition being $\dot{q} = 1.12$ kg/s, the characteristic discharge time approaches $t_d = m_i/\dot{q} = 1000$ s. The characteristic convective time of the jet is $t_c = h/u_{\text{jet}} \approx 2.510^{-4}$ s, taking $u_{\text{jet}} = 300$ m/s. For proper exploitation of the LES, the simulation discussed below corresponds to the range $100 \times t_c < t < 120 \times t_c$, ensuring that no transient effects due to initial or discharge time scales are present: *i.e.* $t_c \ll t \ll t_d$.

The computation begins with still conditions, i.e., the flow is initially at rest in the low pressure reservoir at $P_L = 101325$ Pa, $\rho_L = 1.15$ kg/m^3, and $T_L = 300$ K. The high-pressure tank is $P_H = 4.03 \times P_L$, $\rho_H = 4.03 \times \rho_L$, and $T_H = T_L$, (Fig. 3). Unless specified otherwise, all tank boundaries are assumed to be adiabatic no-slip walls. The turbulent boundary layer inside the nozzle is neglected and adiabatic slip-walls are imposed. The impacted flat plate (vertical plane on Fig. 3) is expected to also have a very thin turbulent boundary layer. Because directly computing the eddies in this region would result in extremely fine grids, a crude approximation is adopted and a simple adiabatic slip-wall condition is used.

The grid convergence analysis uses three unstructured tetrahedra grids, generated for the same geometry (Table 2). The leading parameter is the number of nodes in the diameter of the injector. As the solver is explicit, the time step Δt is limited by the smallest cell size Δx and the fastest acoustic propagation speed $u + c$, with u standing for velocity and c for sound speed (Courant–Friedrichs–Lewy criterion [43]):

$$\Delta t < \text{CFL} \frac{\min(\Delta x)}{\max(u + c)} \tag{1}$$

The explicit scheme is third-order in time and space and yields stable numerical solutions provided that CFL ≤ 0.7 [44].

The grid generation package Centaur[§] is used to generate the three meshes. Throughout the following document, x, y, and z are, respectively, used for the axial, transverse, and spanwise components of the position vector $\mathbf{x}$, while r is used for the radial distance from the jet symmetry axis. Mesh refinement allows a maximum stretching ratio of 1.7 between tetrahedrons and 1.5 between edges. Cell size distribution is depicted in Fig. 4. A uniform grid size is enforced in the region of interest. The jet impact zone is also uniformly discretized for a region defined by $r/d \leq 2$. Finally, a buffer zone imposes linear coarsening for the three meshes away from the impact. All grid characteristics are detailed in Table 2 with their computational costs in Table 3. In this last table, Subscripts cpu (resp. hum.) denotes time used by one processor (resp. human time).

[§]For more information see http://www.centaursoft.com [accessed July 2010].

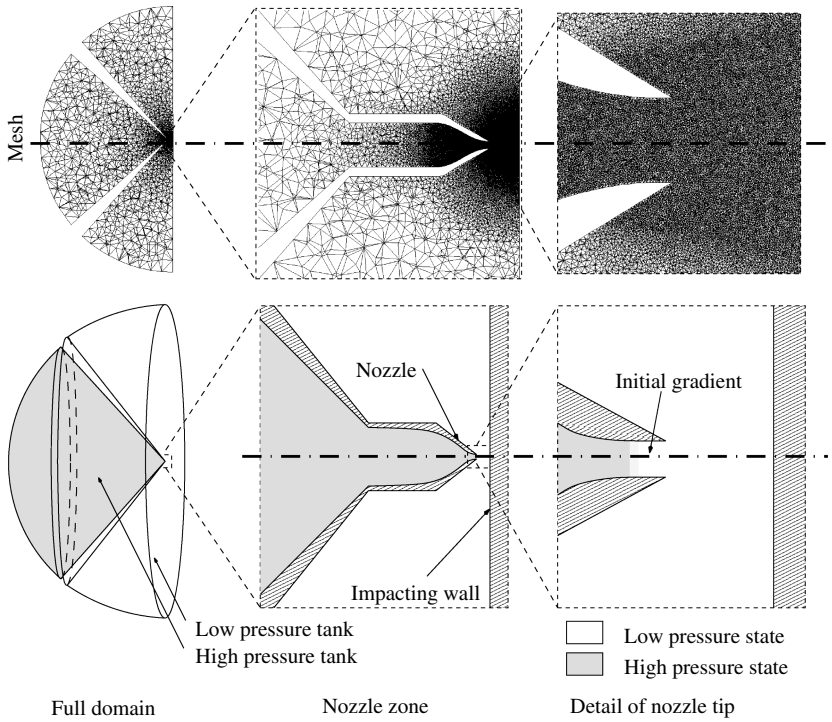

Fig. 3 Computational domain and initial conditions.

B. LES Model

LES involves a spatial filtering operation which reduces for locally, temporally invariant and localized filter functions, to

$$\overline{f(\mathbf{x},t)} = \int_{-\infty}^{+\infty} f(\mathbf{x},t)G(\mathbf{x}'-\mathbf{x})\,\mathrm{d}\mathbf{x}' \tag{2}$$

or using Favre filtered quantities:

$$\widetilde{f(\mathbf{x},t)} = \frac{1}{\bar{\rho}(\mathbf{x},t)}\int_{-\infty}^{+\infty} \rho(\mathbf{x}',t)f(\mathbf{x},t)G(\mathbf{x}'-\mathbf{x})\,\mathrm{d}\mathbf{x}' \tag{3}$$

where G denotes the filter function [45]. Note that implicit filtering is used in the present work, the filter width being approximated by the cell size $\Delta x \overset{3}{=} \sqrt{V}$ with V denoting the local cell volume.

The filtered quantity $\bar{f}$ is resolved in the numerical simulation whereas $f' = f - \bar{f}$ is the subgrid scale part due to the unresolved flow motion. The balance equations for LES are obtained by filtering the intantaneous balance equations yielding to:

$$\frac{\partial \bar{\rho}\tilde{u}_i}{\partial t} + \frac{\partial}{\partial x_j}(\bar{\rho}\tilde{u}_i\tilde{u}_j) = -\frac{\partial}{\partial x_j}[\bar{P}\delta_{ij} - \bar{\tau}_{ij} - \bar{\tau}^t_{ij}] \tag{4}$$

$$\frac{\partial \bar{\rho}\tilde{E}}{\partial t} + \frac{\partial}{\partial x_j}(\bar{\rho}\tilde{E}\,\tilde{u}_j) = -\frac{\partial}{\partial x_j}[\overline{u_i(P\delta_{ij} - \tau_{ij})} - \bar{q}_j - \bar{q}^t_j] \tag{5}$$

where a repeated index implies summation over this index (Einstein's rule of summation). The following symbols ρ, u_i, E, τ, q denote, respectively, density, the velocity vector, the total energy per unit mass, the stress tensor and the heat flux. Superscript t denotes unclosed turbulent terms. The fluid follows the ideal gas law $p = \rho \mathrm{T}R/W_{\mathrm{air}}$ and $e_s = \int_0^T C_p\,\mathrm{d}T - p/\rho$, where T is the temperature, $C_p(T)$ the fluid heat capacity at constant pressure, which is a function of temperature (tabulation of the JANNAF thermodynamical data). The viscous stress tensor and the heat diffusion vector use classical gradient approaches. The fluid viscosity follows Sutherland's law and the heat diffusion follows Fourier's law. Hence

$$\bar{\tau}_{ij} = 2\bar{\rho}\nu\left(\tilde{S}_{ij} - \frac{1}{3}\delta_{ij}\tilde{S}_{ll}\right) \tag{6}$$

where ν is the kinematic viscosity and $\tilde{S}_{ij}$ is the Favre filtered symmetric strain rate tensor. The filtered heat flux $\bar{q}_i$ reads

$$\bar{q}_i = -\lambda\overline{\frac{\partial T}{\partial x_i}} \approx -\frac{\mu\bar{C}_p}{Pr}\frac{\partial \bar{T}}{\partial x_i} \tag{7}$$

with a Prandtl number set to 0.7 for air.

Because of filtering, unclosed terms need to be modeled. The turbulent subgrid stress tensor uses the concept of eddy viscosity

$$\bar{\tau}^t_{ij} = 2\bar{\rho}\nu_t\left(\tilde{S}_{ij} - \frac{1}{3}\delta_{ij}\tilde{S}_{ll}\right) \tag{8}$$

The associated turbulent viscosity is computed according to the Smagorinsky model [46–48]

$$\nu_t = (C_S\Delta x)^2\sqrt{2\tilde{S}_{ij}\tilde{S}_{ij}} \tag{9}$$

with the constant C_S set to 0.18; Δx being the filter size. The turbulent heat flux vector is modeled by

$$\bar{q}^t_i = -\frac{\mu_t\bar{C}_p}{Pr^t}\frac{\partial \tilde{T}}{\partial x_i} \tag{10}$$

with a turbulent Prandtl number Pr^t set to 0.6.

Table 2 Typical mesh characteristics used to assess LES

	$\Delta x/d$	Nodes	Tetrahedra	Memory size	Time step
M20	1/20	1 299 149	7 497 557	147 MB	0, 524 μs
M30	1/30	2 763 143	16 026 453	312 MB	0, 27 μs
M40	1/40	3 833 370	22 280 845	433 MB	0, 214 μs

C. Shock-Capturing Scheme and Artificial Viscosity

The shock pattern present in supersonic jets is one of the main difficulties in LES of high-speed flows [49]. LES solvers able to handle shocks rely on either localized artificial viscosity [50–53], or on spatial schemes adapted to handle discontinuities while preserving the positiveness of the solution, giving birth to a wide family of techniques ranging from the initial approximated Riemann solvers

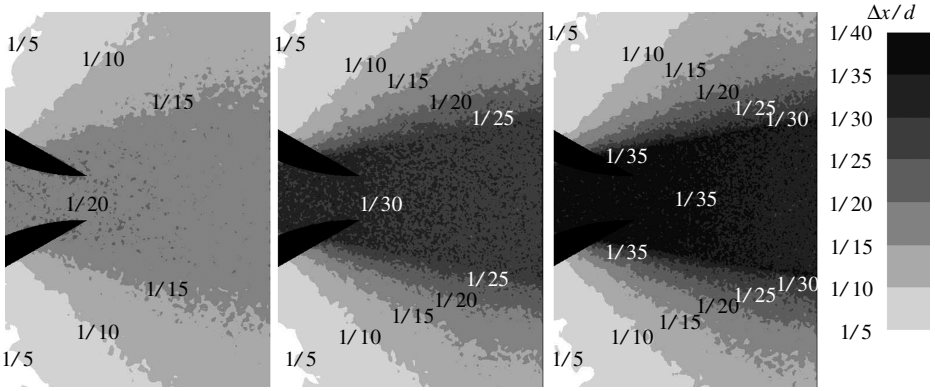

Fig. 4 Local view of the typical nozzle to flat plate mesh resolution as obtained for the three grid: a) the coarse, b) the intermediate, and c) the fine meshes. Isocontours and labels corresponds to the field of $\Delta x/d$.

to the WENO (weighted essentially no oscillatory schemes [54]). WENO schemes are attractive for LES because of their very high precision [40] but imply longer computational time. In the present work, centered schemes were chosen because of their superior performance (low dissipation) in shock-free regions. To preserve the positivity of the solution in regions where strong gradients exist, a hyperviscosity β is introduced in the viscous stress tensor $\bar{\tau}_{ij}$, using the approach of Cook and Cabot [53]. This hyperviscosity may be viewed as an additional pressure term that thickens the shock front

$$\bar{\tau}_{ij}^{\text{modified}} = \left(\beta - \frac{2}{3}\mu\right)\frac{\partial \tilde{u}_k}{\partial x_k} + 2\mu\tilde{S}_{ij} \tag{11}$$

The bulk viscosity β is modeled as

$$\beta = C(\Delta x)^4\nabla^2\|\tilde{S}\| \quad \text{and} \quad \|\tilde{S}\| = (\tilde{S}_{ij}\tilde{S}_{ji})^{1/2} \tag{12}$$

where C is fixed to 5 [55]. This viscosity acts on the very sharp velocity gradients characterizing shocks but goes back to zero in zones where the velocity evolves smoothly [56].

IV. Results and Discussion

The simulation of this stable case is validated by comparing time-averaged and instantaneous LES fields with experimental results. Impact of the mesh resolution on the LES results is studied afterward. This last part includes the observation of instantaneous flow quanties, time-averaged values, and energy distribution through spectral analysis.

A. Mean Flow Topology and Features

Figure 5 presents mean velocity isolines in the median transverse plane (**xy** plane): bottom half is a digital particle imaging velocimetry result by averaging on 400 instantaneous vector fields separated by 1.2 μs, i.e., over 0.48 ms. The DPIV field resolution is around 1 mm or $d/20$. Top half is a LES result on the finest grid M40 obtained by averaging 160 vector fields separated by 57 μs, i.e., over 9.12 ms. Contour lines are drawn using the same procedure, allowing direct quantitative comparisons. Three regions are clearly of interest in this jet configuration. The first region (A) corresponds to the outer part of the jet and is characterized by a low Mach turbulent flow dominated by shear. This subsonic zone, with velocities ranging from 50 to 300 m/s, matches the experiment very well. The LES mixing layer thickness is, however, slightly larger than the experimental one.

Table 3 Cpu-time on 512 processors Intel/Nehalem

One convective time			Total time used	
	$t_{\text{cpu}}^{\text{conv}}$	$t_{\text{hum}}^{\text{conv}}$	$t_{\text{cpu}}^{\text{tot}}$	$t_{\text{hum}}^{\text{tot}}$
M20	82.9 h	9.7 min	17 955 h	35 h
M30	353.8 h	41.5 min	17 412 h	34 h
M40	662.0 h	72.9 min	19 938 h	39 h

The second jet region (B) is dominated by supersonic flow structures with shocks and locates in the inner part of the jet from $x/d = 0$ to $x/d \approx 3.5$. Here most of the velocity patterns agree, confirming the spatial location of the different weak, strong, and reflected shocks (Fig. 1). The two expansion/compression barrels for $x/d < 3$ and a small supersonic tore near $x/d = 3.5$ are reproduced by the numerical approach. The size or the expansion-compression cell Δ_{cell} is $1.5d$ in the simulation and $1.6d$ in the experiment, a value consistent with Powell [42]. A third narrow subsonic region (C) is clearly visible after the Mach disc near the axis in the simulation. This region is mentioned in the experiment:, however, the DPIV resolution makes its quantification difficult. Note that contours are more diffused in the simulation : a small difference or uncertainty in the NPR between experiment and simulation could cause such discrepancies. The major effect of these local differences in the inner supersonic and outer subsonic regions is that the overall jet opening angle differs slightly in LES and in the experiment. The fourth zone of interest (D) is the recirculation bubble which forms along the central axis of the jet in the vicinity of the plate. This subsonic region is characterized by an abrupt deceleration and takes on the shape of a cone whose base is located on the vertical wall: it is very well predicted by LES.

Figure 6 presents an instantaneous isosurface of unit Mach number obtained by LES: longitudinal streaks are clearly visible on the outer rim of the first supersonic cell. This phenomenon has been studied experimentally by Zapryagaev et al. [57,58] and Krothapalli et al. [59]. Geometric singularities on the axisymmetric nozzle give birth to small flow perturbations. These perturbations are amplified downstrean with a Goertler instability triggered by the curved boundary layer. These streaks are stable in space and time in the range $0 < x/d < 1.0$. In the simulation, they stay artificially locked on the perturbations induced spatially by the computational grid. The second observation is the formation of a supersonic hollow disc on the flat wall in the range $1 < r/d < 3$, with supersonic flow islands detaching in the circumferential direction $3 < r/d < 4$.

Figure 7 shows the instantaneous vortical structures present in LES. The isosurface of Q-criterion $Q = 10^{10}$ s^{-2} [60] allows to identify typical jet flow vortices : in the jet plume, the size of such vortices is approximately $d/5$ (about four computational cells) while on the plate, they reach $d/10$ (about 16 computational cells). In the mixing layer, the structures are oblique between the longitudinal axis and the azimuthal direction. Vortices on the wall are aligned azimuthally because of the radial stretching generated by the jet impact on the plate and the flow orientation in this region.

The final zone of interest corresponds to the recirculation bubble in the near wall region and on the jet axis. Donaldson and Snedeker [10] provided a precise visualization of the recirculation bubble shape on the wall for a similar configuration (NPR = 6.76, $h/d = 5.32$, diverging nozzle). The typical streamline pattern of the recirculation

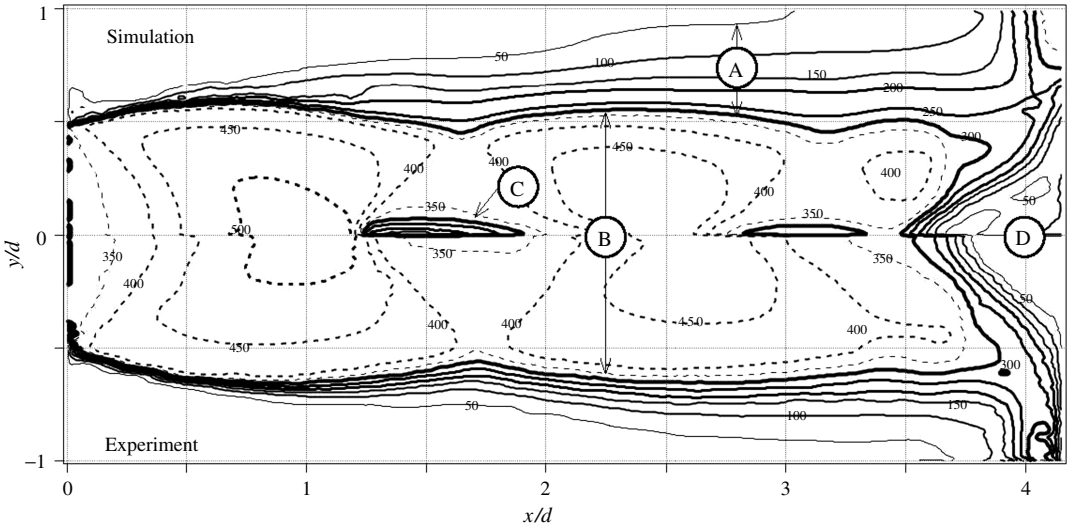

Fig. 5 Comparison of time-averaged velocity fields as obtained by the fine mesh simulation (top half) and experiment (bottom half). Contour values in m/s.

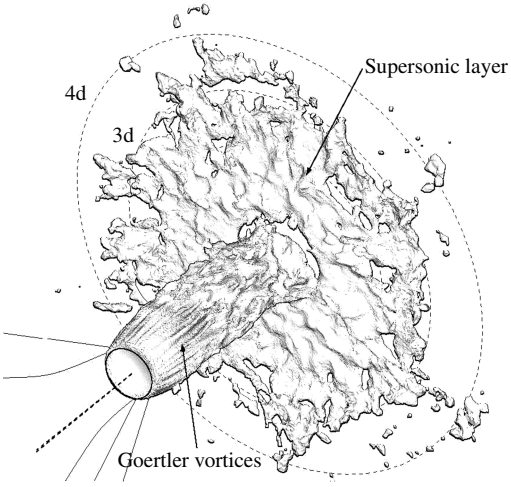

Fig. 6 Instantaneous isosurface of unit Mach number as obtained by LES.

is reproduced on Fig. 8c, based upon the grease streak picture of Fig. 8d. The limit of the recirculation appears as a dividing ring. This ring is divided into segments by several nodes often aligned with nozzle imperfections in Donaldson's experiments. The division can reduce down to three equal segments for a very smooth nozzle (Fig. 8c).

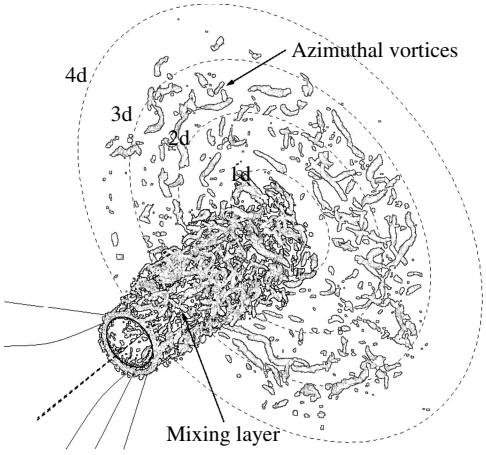

Fig. 7 Instantaneous view of the Q criterium isosurface $Q = 110^{10}$ s^{-2} obtained by LES.

Time-averaged velocity vectors of the simulation near the wall (Fig. 8a) allow a direct comparison with Donaldson's experiments [10]. The pattern is nearly symmetric, showing two similar segments. The center of the bubble is on the diameter linking the two nodes. A flow separation line lies on the diameter. The pattern is not perfectly axisymmetric, i.e., the saddle points are not located in the middle of the segments, and the separation point is not centered. This can be explained either by an averaging time too short compared with the evolution of the bubble, or by the nonperfectly axisymmetric flow upstream, as seen previously on the longitudinal streaks locked on the unstructured mesh.

The pattern is very different on the instantaneous picture (Fig. 8b): the dividing ring moves away from its equilibrium position, in the zone $1 < r/d < 1.5$. There are four nodal points and the segments are variable in shape and size : the recirculation bubble oscillates around a regular shape.

B. Mesh Resolution Effects

Controlling the effects of mesh resolution on LES is a major issue in computational fluid dynamics. As indicated by Pope [61], only statistical results (time-averaged moments for example) are expected to converge when the grid size decreases. Aside from grid resolution, individual realizations in LES depend on rounding errors, compiling options, numbers of processors used on a parallel machine as shown by Senoner et al. [62] and Metais and Lesieur [63]. Therefore, verifying grid effects in LES is a difficult exercice. In the present case, the influence of mesh is tested by repeating the same simulations on three grids containing 7.5, 16, and 22 M cells. For all grids, time-averaged velocity and pressure fields are compared (Sec. IV.B.2). Power spectral densities are also studied in Sec. IV.B.3.

1. Instantaneous Fields

In supersonic jets, different classes of compressible effects are of interest and they all need to be properly evaluated numerically if tone dominated conditions are to be predicted. The first level of compressibility is the generation and location of strong, weak, and reflected shocks. The second level of compressibility can be associated to flow instabilities with the generation of vortical structures and strain. Finally, the third level results from the emission by the flow of acoustic waves propagating in the medium. These effects can be distinguished by the density gradient $\|\nabla\rho\|$ which they induce: strong for shocks, medium for vortices and small for acoustics. Three different black and white scales with different orders of magnitude

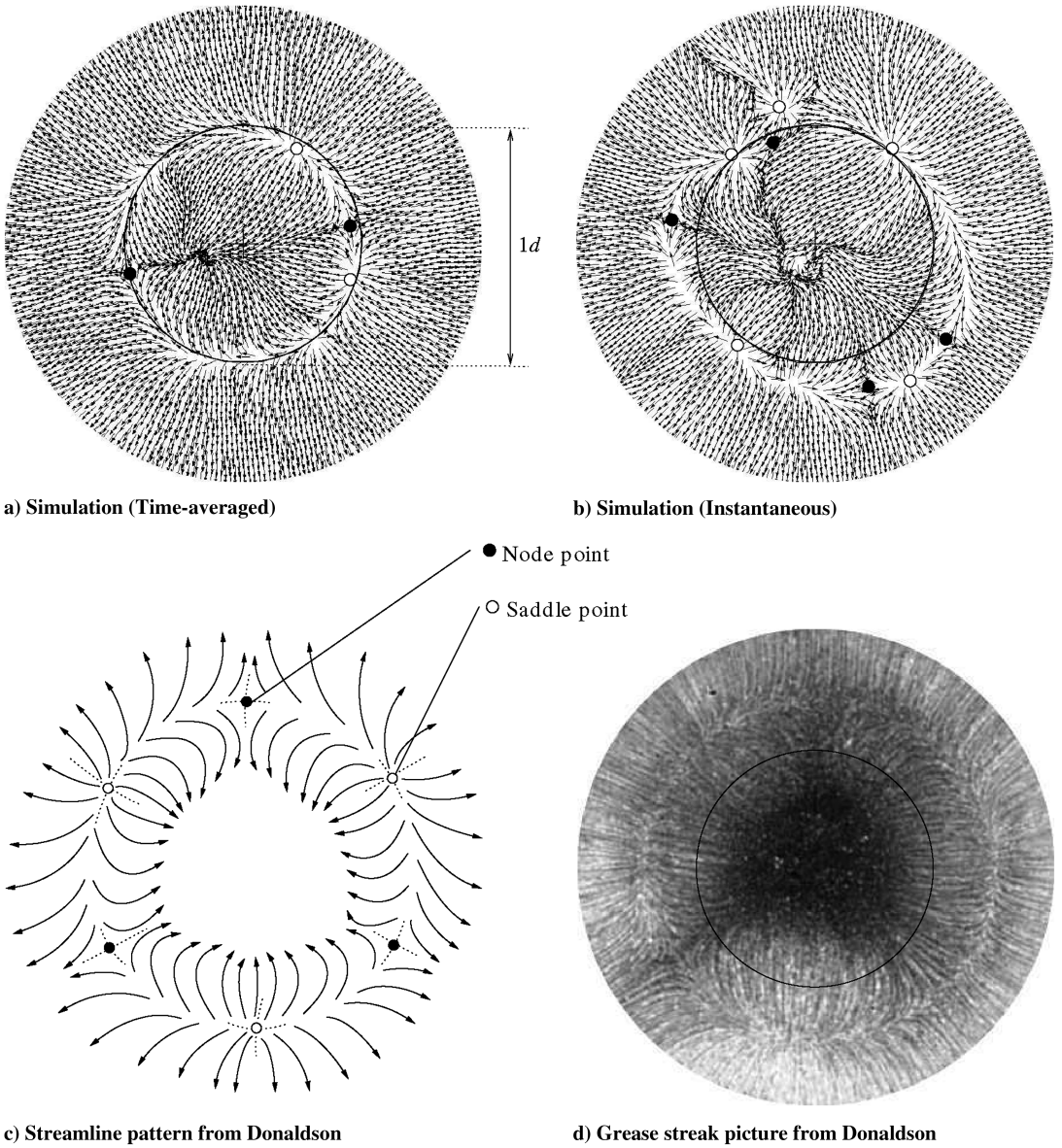

a) Simulation (Time-averaged)

b) Simulation (Instantaneous)

c) Streamline pattern from Donaldson

d) Grease streak picture from Donaldson

Fig. 8 Instantaneous a) and time-averaged b) simulated vector fields on the plate, compared with the sketch c) and grease-streak photograph d) of Donaldson [10].

are shown in Fig. 9 for instantaneous LES fields obtained on the three different meshes.

Based on this diagnostic, simulations M30 and M40 (i.e., intermediate and fine grid resolutions, respectively) appear very similar while simulation M20 (i.e., coarse grid) deviates significantly from the two others due to excessive dissipation; in particular the corrugated shear layer (labeled I in Fig. 9) and the acoustic waves (labeled III in Fig. 9) are excessively smeared on M20 (Fig. 9a).

An illustration of the instantaneous Mach number distribution for the three grid resolutions at the same instant is given in Fig. 10. The coarse grid LES M20 clearly attenuates most of the dynamics. It is able to place properly the different inner jet supersonic structures but produces highly damped unsteady motions in the outer jet mixing layers and along the plate. An increase of resolution improves the local sharpness of the different structures as observed on M30. The fine grid resolution M40 reveals more intermittency in the Mach distribution especially along the plate as well as sharper supersonic patterns in the inner jet region.

As expected with LES, as the local grid resolution increases, more flow structures are explicitly resolved and the resolved flow energy content is increased. It must be compared with dissipation effects due to artificial viscosity, shock-capturing, and flow laminar or turbulent viscosities. These questions are investigated below using instantaneous views of various ratios of viscosities for three grid resolutions.

The artificial viscosity ($\mu_{\text{A.V.}}$) resulting from the shock-capturing scheme and the necessary numerical stabilization is given in Fig. 11. For all meshes, artificial damping is low and localized along shear layers and shock lines. Compared with the laminar contribution the ratio remains low: it exceeds unity on M40 only in zones of shocks, something which can not be avoided. Simulations M30 and M40 exhibit similar results, with artificial viscosity lower than the laminar 1 in.some parts of the jet (Figs. 11b and 11c): in the range 1–10 on the shear layer and around 10 on the shock lines. Note nonetheless that LES with M20 yields significantly more damped supersonic structures, in agreement with an artificial to laminar viscosity ratio, which saturates around 10 in the core of the jet (Fig. 11a). Nozzle lip, Mach disc and top of recirculation bubble are the most damped regions with a ratio close to 30 for all meshes. From a numerical point of view, Fig. 11 confirms the correct behavior of the strategy devised to handle such flows with LES. The dissipation ratio is approximated at the first order by the ratio of viscosities. The reader can refer to [64–66] for an extensive discussion on the computation of dissipation induced by the LES models. As the mesh resolution increases, the zones where artificial viscosity is added reduce in intensity and become highly localized.

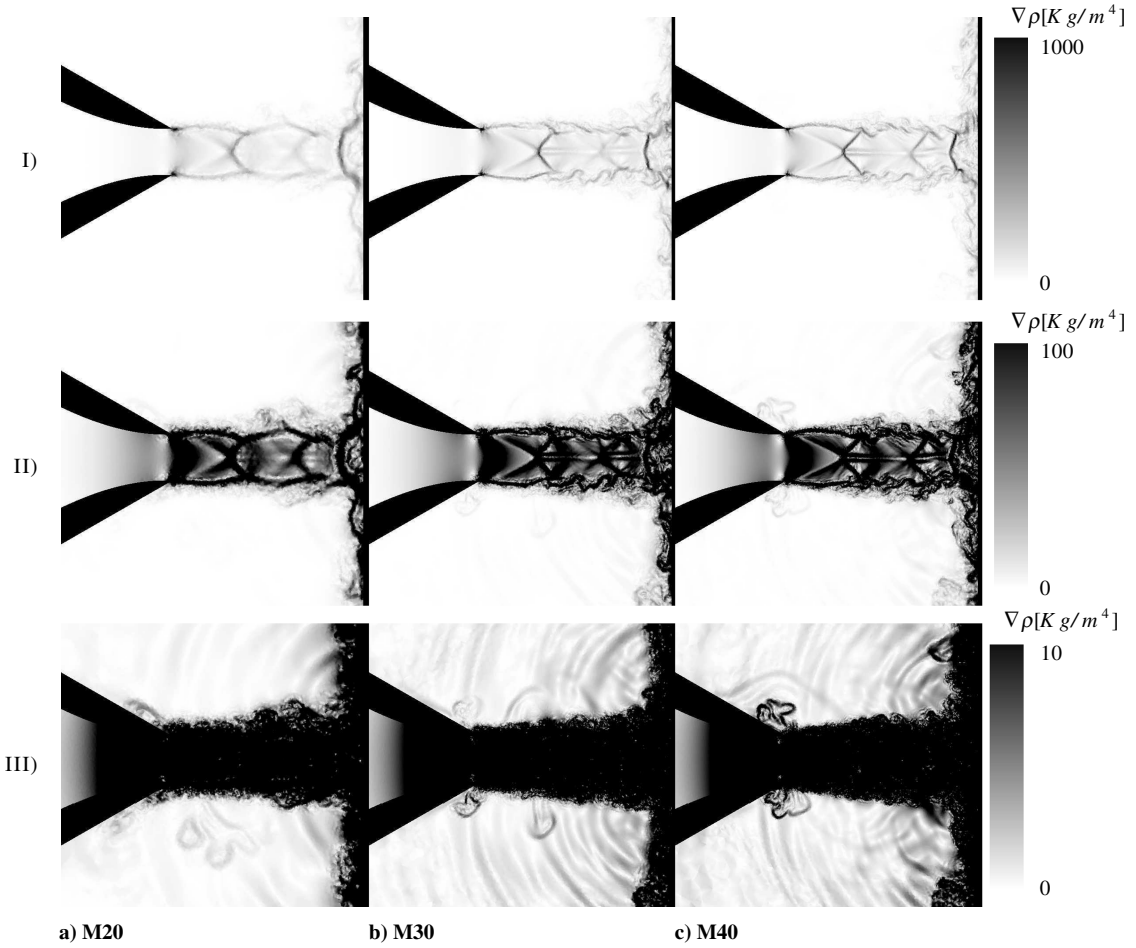

Fig. 9 Magnitude of the density gradient for three ranges of scale and for the same instantaneous field obtained on the three meshes at the same instant. Top I: large values, supersonic patterns; middle II: intermediate values, shear layers; bottom III: small values, acoustic waves. The diagnostic is provided for the xy plane going through the central axis of the jet.

The turbulent viscosity $\mu_{\text{Turb.}}$ to laminar viscosity ratio is provided on Fig. 12 and is to be compared with Fig. 11 for the same grids: $\mu_{\text{Turb.}}$ is created in regions of high shear and strain, meeting the requirement of LES. Its intensity reaches values ranging from 10 to 40 times the laminar viscosity in the turbulent zones and is roughly 10 times superior to the artificial viscosity levels of Fig. 11. Simulations M30 and M40 yield a ratio $\mu_{\text{Turb.}}/\mu_{\text{Lam.}}$ close to 10 in the shear layer of the jet (Figs. 12b and 12c) while simulation M20 shows higher levels of turbulent viscosity (closer to 100) over the entire shear layer (Fig. 12a).

To summarize, Mach number and density gradient fields are similar for meshes M30 and M40. Artificial and turbulent viscosity levels are reasonable and localized in shock and shear regions.

2. Mean Quantities

Time-averaged values are obtained in the range $80 < t/t_c < 100$ with a sampling close to $0.1 \times t_c$ and compared for the three meshes M20, M30, and M40. For notation, $\langle u\rangle_{\text{mean}}$ (resp. $\langle p\rangle_{\text{mean}}$) is the time-averaged value of the velocity u (resp. pressure p), and $\langle u\rangle_{\text{rms}}$ denotes root mean square velocity of the resolved field, without defiltering technique or subgrid model inclusion [67].

The longitudinal profiles of pressure and velocity are displayed on Fig. 13. The velocity fields estimated from digital particle imaging velocimetry (DPIV) in Henderson's experiment [7] are compared with the three simulations in Fig. 13a. The two high-velocity zones for $x/d = 1$ and $x/d = 2.5$ are well reproduced. Simulations M30 and M40 both show a strong deceleration after these high-speed

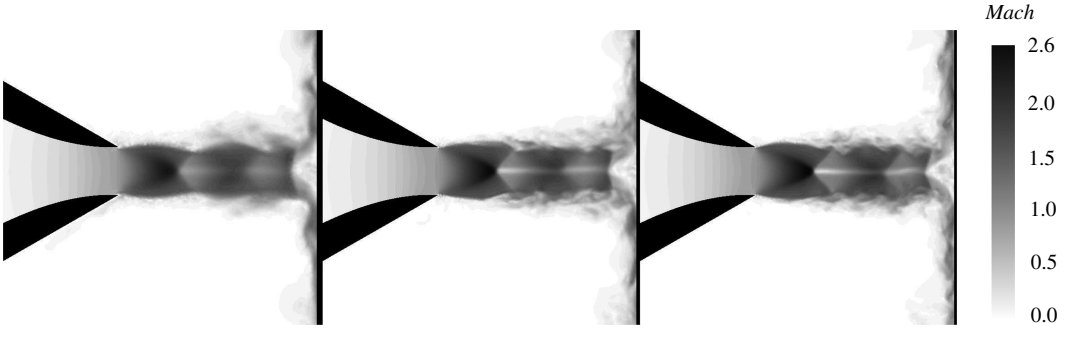

Fig. 10 Instantaneous Mach number field as obtained on the three meshes. The diagnostic is provided for the *xy* plane going through the central axis of the jet.

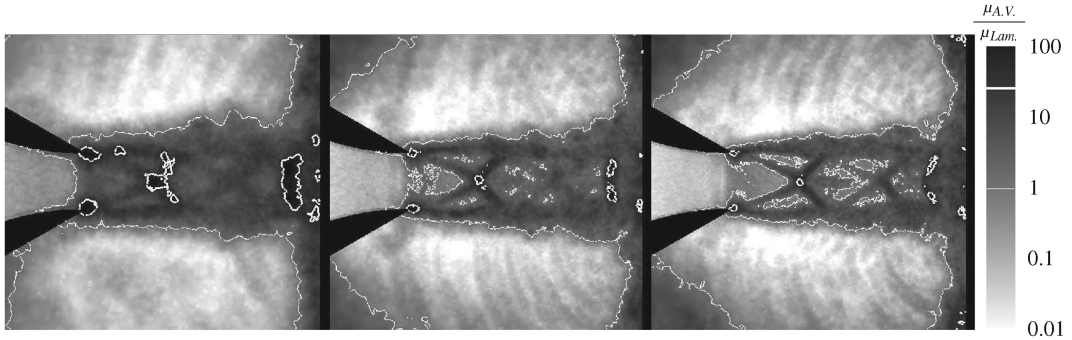

a) M20 b) M30 c) M40

Fig. 11 Field of ratio of artificial viscosity to laminar viscosity. White contours are drawn for ratios equal to unity (thin line) and 30 (bold line).

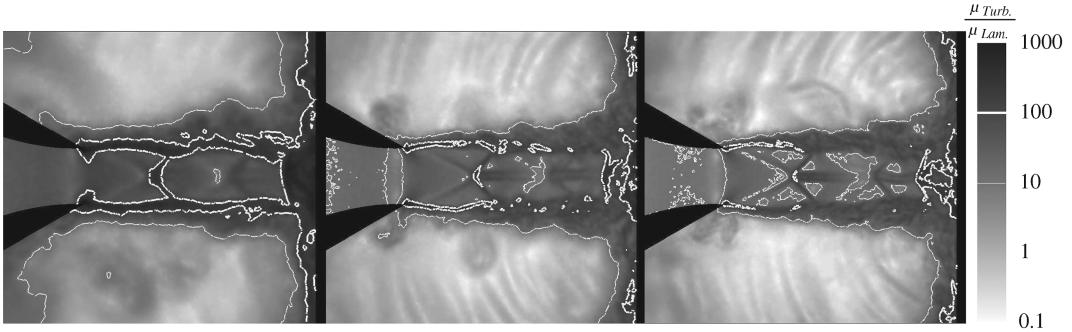

a) M20 b) M30 c) M40

Fig. 12 Field of ratio of turbulent viscosity to laminar viscosity. White contour are drawn for ratios equal to 10 (thin line) and 100 (bold line).

zones, while simulation M20 is apparently closer to experimental observations. This gap can be explained both by the underestimation of the turbulence behind the Mach disc in the simulation and bias of DPIV in strong deceleration and sharp gradients. For example, the subsonic bubble visible in Fig. 5 has a diameter of $0.1d = 2.54$ mm while the spatial resolution of the DPIV is 1 mm: the same profile taken 1 mm away from the axis would not show the axial subsonic zone. Time-averaged pressure is decreasing in the recirculation

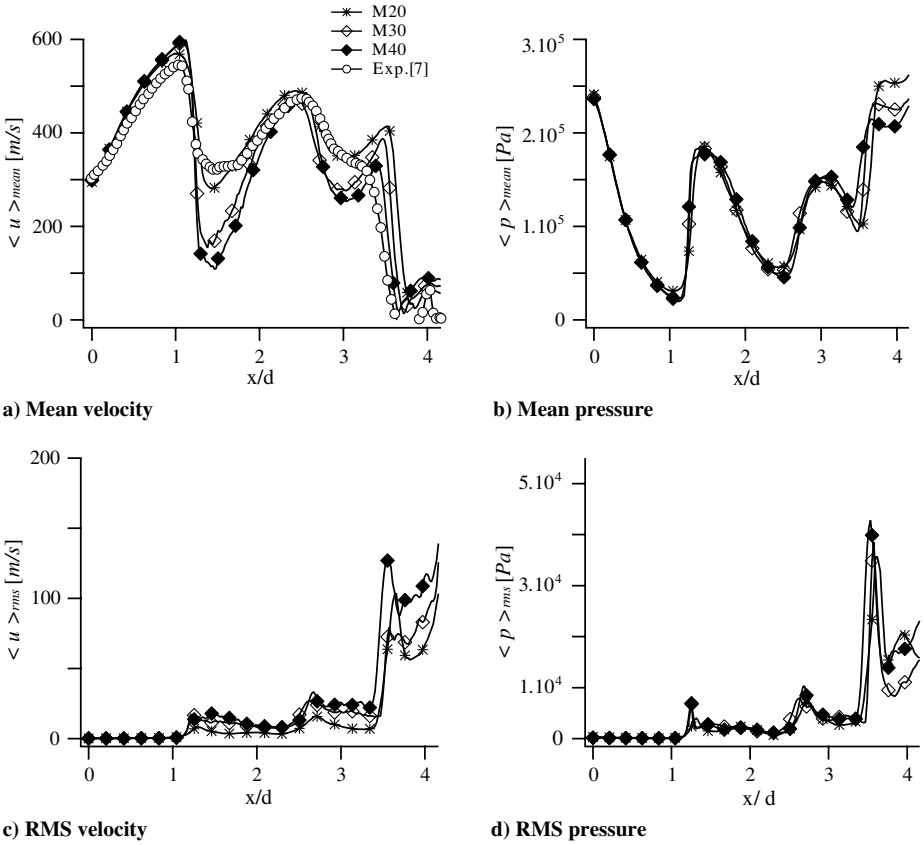

a) Mean velocity b) Mean pressure

c) RMS velocity d) RMS pressure

Fig. 13 Time-averaged velocity: a) time-averaged static pressure, b) rms fluctuation of velocity, c) rms fluctuation of pressure, and d) along the axis of the jet.

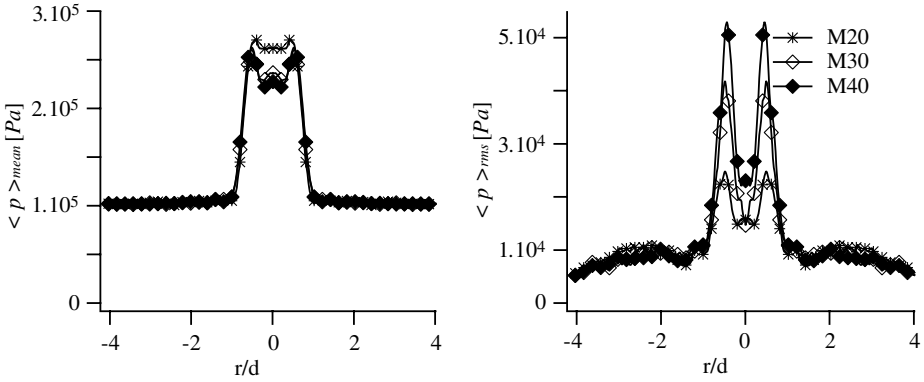

a) Mean pressure **b) R.M.S. pressure**

Fig. 14 Pressure profile at the wall.

zone: a better resolution of strong shocks yields stronger pressure loss, and a lower static pressure on the wall.

The time-averaged pressure, rms velocity, and rms pressure (resp. Figures 13b–13d) all show a good agreement. In the recirculation zone, for $x/d > 3.5$, velocity and pressure fluctuations vary by approximately 20% when the resolution increases.

In Fig. 14, radial profiles are averaged over several radial directions to get a better statistical convergence of the profiles and relying on the axisymmetric nature of the flow. Time-averaged static pressure distributions on the impinging wall are given on Fig. 14a. It shows a very good grid convergence between simulations M20, M30, and M40. The pressure fluctuation, in Fig. 14b, shows the same convergence, except for the peaks at $r = \pm 0.5d$ where simulation M40 exhibits fluctuations which are 20% higher than simulation M30.

First-order moments for velocity and pressure show satisfactory agreement with respect to grid resolution (Figs. 13a, 13b, and 14a): a first-order convergence is achieved. Second-order moments converge too but more slowly in the recirculation bubble.

3. *Spectral Analysis*

The energy content of the resolved scales can be quantified by means of spectral estimators to investigate the evolution of the energy distribution with respect to the grid resolution.

A common first-order spectral estimator is the sound pressure level (SPL) distribution of a pressure signal versus the frequency f. For a location $\mathbf{x}$, the pressure signal is sampled each 10 μs for ten different radial directions in **yz** planes. The following results are averaged azimuthally over these 10 locations. This averaging process is denoted $\langle\,\rangle_{\text{az.}}$. The Fourier transform of pressure is denoted $\hat{p}_x$. Note that this transformation involves chronologically: 1) a resampling of the datasets to ensure a fixed time step, 2) a removal of the linear trends, 3) a low-pass filtering removing frequencies above 40% times the Nyquist frequency, and 4) Hanning windowing. The windowing is done for the ten locations before azimuthal averaging $\langle\,\rangle_{\text{az.}}$. The Nyquist frequency approaches 100 kHz for all signals. Care has been taken that all segments present the same first and second statistical moments within a 10% tolerance. With the adequate normalization, the norm of the Fourier transform gives the amplitude of each harmonic depending on the frequency $A_x(f)$, Eq. (13). Sound pressure level is defined as the root mean square of each harmonic normalized by the reference 20 μPa, and often expressed in decibels, as in Eq. (14)

$$A_x(f) \equiv \langle \sqrt{\hat{p}_x \hat{p}_x^*} \rangle_{\text{az.}} \tag{13}$$

$$\text{SPL}_x(f) \equiv 20 \log\left(\frac{A_x \times \sqrt{2}/2}{20\ \mu\text{Pa}}\right) \tag{14}$$

The spectrum is built for four different locations: Impact, Middle, Lip, and Acoustic, which are detailed in Fig. 15. Going from the highest to the lowest energy content, the spectral analysis yields:

1) Impact: on the impact plate (Fig. 16a) where the strongest pressure fluctuations occur. SPL is above 160 dB in the range 0–10 kHz. A weak maximum is found for both mesh M30 and M40 at the frequency 6 kHz, corresponding to a rms fluctuation near 4000 Pa. The energy content decreases slowly for the high frequencies.

2) Middle: in the middle of the jet, near the Mach disc (Fig. 16b), the energy content is almost constant near 140 dB, i.e., a rms fluctuation around 200 Pa.

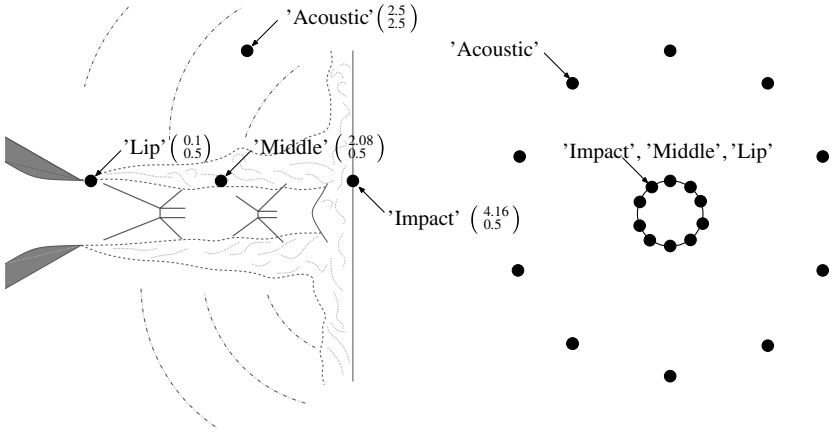

Fig. 15 Locations used for spectral analysis. Coordinates are specified as $\binom{x/d}{r/d}$.

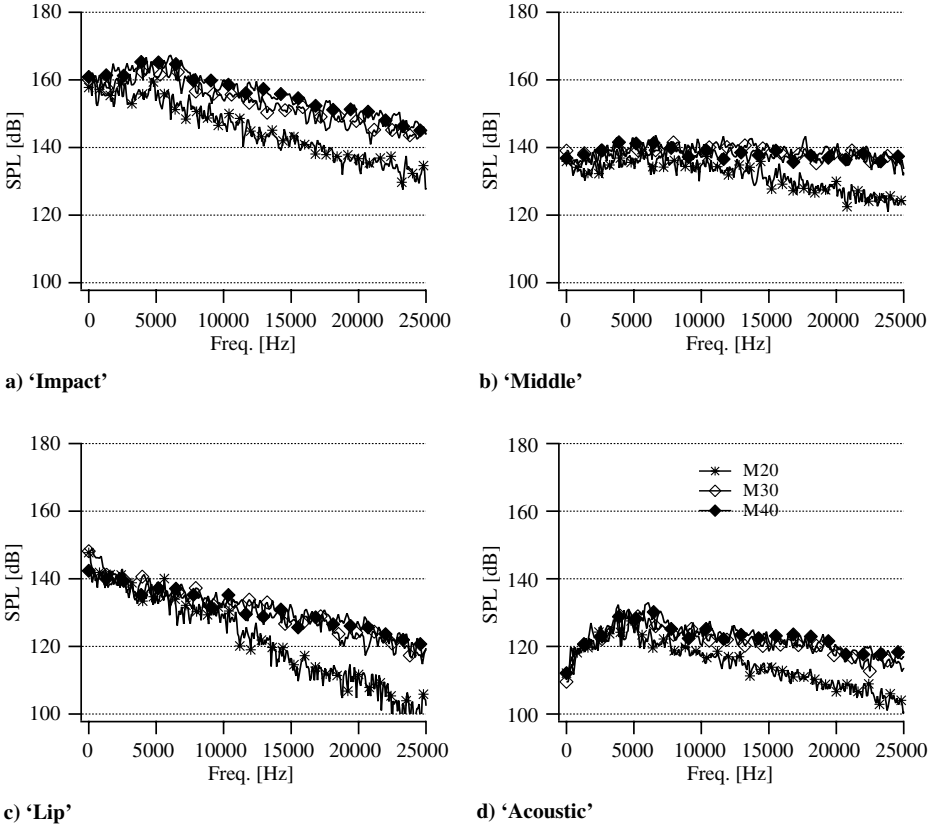

Fig. 16 Averaged energy spectra.

3) Lip: at the nozzle lip (Fig. 16c), the maximum energy starts at 140 dB in the lowest frequency range and decreases smoothly toward 120 dB for 25 kHz (100 dB for mesh M20).

4) Acoustic: In the zone at rest, to isolate propagating acoustic waves (Fig. 16d), the energy distribution is comparable to the impact zone. The SPL rises in the range 0–6 kHz from 100 to 140 dB, then decreases on the range 6–20 kHz down to 120 dB (110 dB for mesh M20).

The spectra are very different in terms of energy distribution and amplitude (Fig. 16). However, a clear convergence is established between simulations M30 and M40. The simulation M20 shows in all cases an energetic content 10 dB lower than the two finer grids. The most important discrepancy between simulation M30 an M40 is observed in the impact region, Fig. 16a with a shift of 3 dB/Hz. This shift can be linked to the pressure fluctuations, stronger with the simulation M40. This discrepancy has no impact on the energy spectra at the three other locations. In spite of a maximum amplitude reached for 6 kHz, there is no discrete tone production in this case, as expected from experiments.

Involving nonlinear products, the two-point estimators are part of second-order spectral analyses. The interspectrum S_{xy} between the pressure signals of locations **x** and **y** is normalized by the autospectra of both signals S_{xx} and S_{yy}, yielding the coherence estimator:

$$\mathrm{Coh}_{xy} \equiv \left\langle \frac{|S_{xy}|}{\sqrt{|S_{xx}||S_{yy}|}} \right\rangle_{\mathrm{az.}} \equiv \left\langle \frac{\sqrt{\hat{p}_x \hat{p}_y^*}}{\sqrt{\hat{p}_x \hat{p}_x^* \hat{p}_y \hat{p}_y^*}} \right\rangle_{\mathrm{az.}} \tag{15}$$

This quantity equals one when the output signal p_y is linearly dependent of the input signal p_x. This quantity is decreasing when 1) noise is jamming the measures, 2) the signals are nonlinearly dependent, and 3) the output signal p_y is reacting to more inputs different from p_x. When applied to signals known to be linearly dependent, coherence is a good estimator of the signal-to-noise ratio. The phase of the interspectrum Φ_{xy} defined in Eq. (16) gives the time shift between the signals:

$$\Phi_{xy} \equiv \Phi\langle S_{xy}\rangle_{\mathrm{az.}} \equiv \langle \hat{p}_x \hat{p}_y^* \rangle_{\mathrm{az.}} \tag{16}$$

Note that when two signals are strongly correlated at all frequencies, the time shift is a linear function of the frequency. The slope of this linear function depends on the propagation speed of the signal and the distance between the two locations.

These tools are first applied to a couple of sensors showing almost no correlation. The fluctuations on the wall at the edge of the recirculation zone are probably one of the strong acoustic sources in this flow. As there is no discrete tone production, the response of the jet to acoustics is expected to be low. Therefore, the locations Impact and Lip are expected to be uncorrelated. The two-point phase estimator shown on Fig. 17a shows strictly no linear trend between the two locations. The coherence estimator illustrated on Fig. 17b stays globally below 0.5 for the frequency range [0–20 kHz]. There is therefore no clear linear dependence between a point on the lip and is projection on the impacting wall. Note that coherence seems to get slightly lower with mesh refinement. However, the results are globally independent of the grid.

The two-point estimators are then applied to a couple of locations expected to be strongly correlated. Indeed, the Acoustic location must be directly perturbated by the Impact zone. A clear linear trend is visible in Fig. 18a. The linear slope is roughly estimated by a phase shift of 2π rad, each 5000 Hz. This can be compared with an ideal acoustic propagation. The distance between the two locations is 65.96 mm and the sound propagates at a constant velocity of 347 m/s. Therefore, the time lag between the two signals is 189 μs. In other words, an ideal acoustic propagation gives a 2π phase shift each 5275 Hz. This ideal phase shift is superimposed to the numerical results of Fig. 18a. The linear trend gets sharper with mesh resolution, and is in very good agreement with the ideal acoustic propagation. The coherence is different than the previous case with much higher values in the frequency range [0–10 kHz]. In particular, the finest grid shows values close to unity near 5 kHz. This result underlines a linear dependence between a point in the vicinity of the jet and a point on the wall as we could expect with a purely acoustic

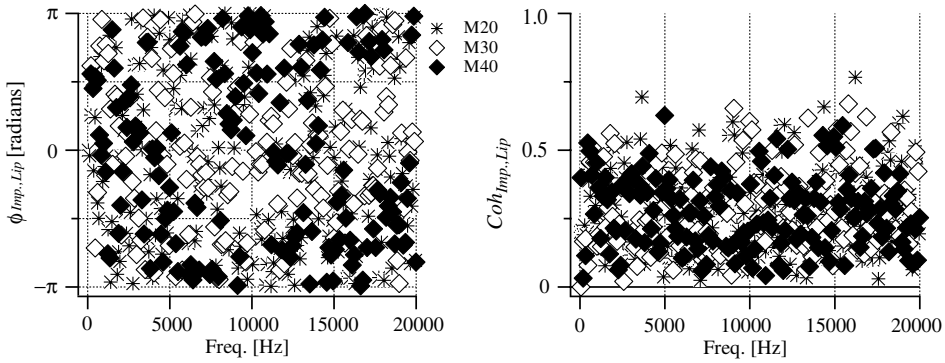

a) Phase shift **b) Coherence**

Fig. 17 No correlation: interspectrum between impact and lip locations.

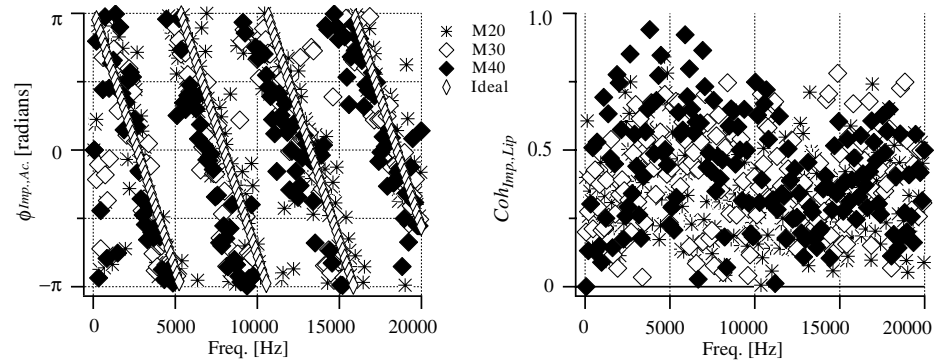

a) Phase shift **b) Coherence**

Fig. 18 Strong correlation: interspectrum between impact and acoustic locations.

propagation of the information. A subsequent result is that the finest grid shows a very good signal-to-noise ratio, i.e., good quality measurements for a spectral analysis in the frequency range [0–10 kHz].

To conclude, the comparison of one-point estimators shows that simulation M30 gives a correct energy distribution. The two-point estimators show a clear interaction between the impact zone and the acoustic field, in spite of a large difference of intensity between the two signals (30 dB). Moreover, one- and two-point estimator results are unchanged between meshes M30 and M40.

V. Conclusions

LES of a supersonic jet impinging on a flat plate in a stable regime is performed with an explicit third-order compressible solver using an unstructured mesh and the Smagorinsky model. Overall and with most of the grid resolutions targeted in this work, the numerical predictions show very satisfactory agreement with experiment observations. To assess the potential effects of various LES parameters, the three levels of mesh refinement are compared in terms of instantaneous and averaged flowfields (shocks and recirculation zone positions), averaged flow velocity and pressure fields, wall pressure, rms pressure fields, and spectral content. In this specific context, the effects of numerical and turbulent viscosities are compared on the three grids and shown to be well controlled. The results also highlight the accessibility of one- and two-point spectral analyses, which, for sufficient grid resolution, are independent of the mesh. To conclude, the finest grid used here (a 22 Mcell mesh) is sufficient to ensure grid-independent results and offer a coherent framework to investigate by use of LES more complex mechanisms on this type of flow, i.e., self-excited tones.

Acknowledgments

Authors acknowledge the Grand 'equipement national de calcul intensif Grand Challenge 2009 team of the Commissariat à l'énergie atomique for making available the Bull hybrid computer titane resources and G. Staffelbach for his technical support in porting the AVBP solver on this new architecture. The authors wish to thank A. Sevrain of Institut de m'ecanique des fluides de Toulouse for his contribution on spectral analysis, and B. Henderson for the information and experimental data provided for this study.

References

[1] Roux, A., Reichstadt, S., Bertier, N., Gicquel, L. Y. M., Vuillot, F., and Poinsot, T., "Comparison of Numerical Methods and Combustion Models for LES of a Ramjet," *Comptes Rendus Hebdomadaires des Seances de l'Academie des Sciences*, Vol. 337, Nos. 6–7, 2009, pp. 352–361.

[2] Wolf, P., Staffelbach, G., Roux, A., Gicquel, L., Poinsot, T., and Moureau, V., "Massively Parallel LES of Azimuthal Thermo-Acoustic Instabilities in Annular Gas Turbines," *Comptes Rendus Hebdomadaires des Seances de l'Academie des Sciences*, Vol. 337, Nos. 6–7, 2009, pp. 385–394.

[3] Roux, S., Cazalens, M., and Poinsot, T., "Influence of Outlet Boundary Condition for Large Eddy Simulation of Combustion Instabilities in Gas Turbine," *Journal of Propulsion and Power*, Vol. 24, No. 3, 2008, pp. 541–546. doi:10.2514/1.33739

[4] Staffelbach, G., Gicquel, L., Boudier, G., and Poinsot, T., "Large Eddy Simulation of Self-Excited Azimuthal Modes in Annular Combustors," *Proceedings of the Combustion Institute*, Vol. 32, Elsevier, New York, 2009, pp. 2909–2916.

[5] James, S., Zhu, J., and Anand, M., "LES of Turbulent Flames Using the Filtered Density Function Model," *Proceedings of the Combustion Institute*, Vol. 31, Elsevier, New York, 2007, pp. 1737–1745. doi:10.1016/j.proci.2006.07.160

[6] Inman, J. A. W., Danehy, P. M., Nowak, R. J., and Alderfer, D. W., "Fluorescence Imaging Study of Impinging Underexpanded Jets," *46th AIAA Aerospace Sciences Meeting and Exhibit*, AIAA, Reston, VA, 2008.

[7] Henderson, B., Bridges, J., and Wernet, M., "An Experimental Study of the Oscillatory Flow Structure of Tone-Producing Supersonic

Impinging Jets," *Journal of Fluid Mechanics*, Vol. 542, No. -1, 2005, pp. 115–137.
doi:10.1017/S0022112005006385

[8] Henderson, B., and Powell, A., "Sound-Production Mechanisms of the Axisymmetric Choked Jet Impinging on Small Plates: The Production of Primary Tones," *Journal of the Acoustical Society of America*, Vol. 99, No. 1, 1996, p. 153.
doi:10.1121/1.414499

[9] Henderson, B., "The Connection Between Sound Production and Jet Structure of the Supersonic Impinging Jet," *Journal of the Acoustical Society of America*, Vol. 111, No. 2, 2002, p. 735.
doi:10.1121/1.1436069

[10] Donaldson, C. D., and Snedeker, R. S., "A Study of Free Jet Impingement. Part 1. Mean Properties of Free and Impinging Jets," *Journal of Fluid Mechanics*, Vol. 45, No. 2, 1971, pp. 281–319.
doi:10.1017/S0022112071000053

[11] Donaldson, C. D., Snedeker, R. S., and Margolis, D. P., "A Study of Free Jet Impingement. Part 2. Free Jet Turbulent Structure and Impingement Heat Transfer," *Journal of Fluid Mechanics*, Vol. 45, No. 3, 1971, pp. 477–512.
doi:10.1017/S0022112071000156

[12] Lamont, P. J., and Hunt, B. L., "The Impingement of Underexpanded, Axisymmetric Jets on Perpendicular and Inclined Flat Plates," *Journal of Fluid Mechanics*, Vol. 100, No. 3, 1980, pp. 471–511.
doi:10.1017/S0022112080001255

[13] Ho, C.-M., and Nosseir, N. S., "Dynamics of an Impinging Jet. Part 1. The Feedback Phenomenon," *Journal of Fluid Mechanics*, Vol. 105, No. 1, 1981, pp. 119–142.
doi:10.1017/S0022112081003133

[14] Kuo, C.-Y., and Dowling, A. P., "Oscillations of a Moderately Underexpanded Choked Jet Impinging Upon a Flat Plate," *Journal of Fluid Mechanics*, Vol. 315, No. 1, 1996, pp. 267–291.
doi:10.1017/S002211209600242X

[15] Berland, J., Bogey, C., and Bailly, C., "Numerical study of screech generation in a planar supersonic jet," *Physics of Fluids*, Vol. 19, No. 7, 2007, p. 075105.
doi:10.1063/1.2747225

[16] Larchevêque, L., Sagaut, P., Le, T., and Comte, P., "Large-Eddy Simulation of a Compressible Flow in a Three-Dimensional Open Cavity at High Reynolds Number," *Journal of Fluid Mechanics*, Vol. 516, No. 1, 2004, pp. 265–301.
doi:10.1017/S0022112004000709

[17] Ferri, A., *Elements of Aerodynamics of Supersonic Flows*, Macmillan Co., New York, 1949.

[18] Adamson, T. C., "Approximate Methods for Calculating the Structure of Jets from Highly Underexpanded Nozzles," BAMIRAC, Tech. Rept.3768-26-T , 1961.

[19] Hsu, A., and Liou, M., "Computational Analysis of Underexpanded Jets in the Hypersonic Regime," *Journal of Propulsion and Power*, Vol. 7, No. 2, 1991, pp. 297–299.
doi:10.2514/3.23324

[20] Birkby, P., Dent, J., and Page, G., "CFD Prediction of Turbulent Sonic Underexpanded Jets," *Proceedings of the 1996 ASME Fluids Engineering Summer Meeting, Pt. 2*, American Society of Mechanical Engineers, Fairfield, NJ, 1996, pp. 465–470.

[21] Cumber, P., Fairweather, M., Falle, S., and Giddings, J., "Predictions of the Structure of Turbulent, Highly Underexpanded Jets," *Journal of Fluids Engineering*, Vol. 117, No. 4, 1995, pp. 599–604.
doi:10.1115/1.2817309

[22] Gribben, B. J., Badcock, K. J., and Richards, B. E., "Numerical Study of Shock-Reflection Hysteresis in an Underexpanded Jet," *AIAA Journal*, Vol. 38, 2000, pp. 275–283.
doi:10.2514/2.954

[23] Prudhomme, S., and Haj-Hariri, H., "Investigation of Supersonic Underexpanded Jets Using Adaptive Unstructured Finite Elements," *Finite Elements in Analysis and Design*, Vol. 17, No. 1, 1994, pp. 21–40.
doi:10.1016/0168-874X(94)90018-3

[24] Sakakibara, Y., and Iwamoto, J., "Numerical Study of Oscillation Mechanism in Underexpanded Jet Impinging on Plate," *Journal of Fluids Engineering*, Vol. 120, No. 3, 1998, p. 477.
doi:10.1115/1.2820687

[25] Alvi, F. S., Ladd, J. A., and Bower, W. W., "Experimental and Computational Investigation of Supersonic Impinging Jets," *AIAA Journal*, Vol. 40, No. 4, 2002, pp. 599–609.
doi:10.2514/2.1709

[26] Shen, H., and Tam, C. K. W., "Three-Dimensional Numerical Simulation of the Jet Screech Phenomenon," *AIAA Journal*, Vol. 40, No. 1, 2002, pp. 33–41.
doi:10.2514/2.1638

[27] Arunajatesan, S., and Sinha, N., "Large Eddy Simulations of Supersonic Impinging Jet Flow Fields," AIAA 2002–4287, 2002.

[28] Berland, J., Bogey, C., and Bailly, C., "Large Eddy Simulation of Screech Tone Generation in a Planar Underexpanded Jet," *12th AIAA/CEAS Aeroacoustics Conference*, AIAA, Reston, VA, 2006, pp. 8–10.

[29] Al-Qadi, I., and Scott, J., "High-Order Three-Dimensional Numerical Simulation of a Supersonic Rectangular Jet," AIAA 2003–3238, 2003.

[30] Bodony, D. J., and Lele, S. K., "On Using Large-Eddy Simulation for the Prediction of Noise from Cold and Heated Turbulent Jets," *Physics of Fluids*, Vol. 17, No. 8, 2005, p. 5103.
doi:10.1063/1.2001689

[31] Bogey, C., and Bailly, C., "Computation of a High Reynolds Number Jet and its Radiated Noise Using Large Eddy Simulation Based on Explicit Filtering," *Computers and Fluids*, Vol. 35, No. 10, 2006, pp. 1344–1358.
doi:10.1016/j.compfluid.2005.04.008

[32] Bogey, C., and Bailly, C., "Investigation of Downstream and Sideline Subsonic Jet Noise Using Large Eddy Simulations," *Theoretical and Computational Fluid Dynamics*, Vol. 20, No. 1, 2006, pp. 23–40.
doi:10.1007/s00162-005-0005-7

[33] Georgiadis, N., Alexander, J., and Reshotko, E., "Hybrid Reynolds-Averaged Navier–Stokes/Large-Eddy Simulations of Supersonic Turbulent Mixing," *AIAA Journal*, Vol. 41, No. 2, 2003, pp. 218–229.
doi:10.2514/2.1934

[34] Chauvet, N., Deck, S., and Jacquin, L., "Shock Patterns in a Slightly Underexpanded Sonic Jet Controlled By Radial Injections," *Physics of Fluids*, Vol. 19, No. 4, 2007, p. 048104.
doi:10.1063/1.2720836

[35] Piomelli, U., "Wall-Layer Models for Large-Eddy Simulations," *Progress in Aerospace Sciences*, Vol. 44, No. 6, 2008, pp. 437–446.
doi:10.1016/j.paerosci.2008.06.001

[36] Georgiadis, N., Alexander, J., and Reshotko, E., "Development of a Hybrid RANS/LES Method for Compressible Mixing Layer Simulations," AIAA 2001–0289.

[37] Cheng, T., and Lee, K., "Numerical Simulations of Underexpanded Supersonic Jet and Free Shear Layer Using WENO Schemes," *International Journal of Heat and Fluid Flow*, Vol. 26, No. 5, 2005, pp. 755–770.
doi:10.1016/j.ijheatfluidflow.2005.01.006

[38] Chauvet, N., Deck, S., and Jacquin, L., "Zonal Detached Eddy Simulation of a Controlled Propulsive Jet," *AIAA Journal*, Vol. 45, No. 10, 2007, p. 2458.
doi:10.2514/1.28562

[39] Chauvet, N., Deck, S., and Jacquin, L., "Numerical Study of Mixing Enhancement in a Supersonic Round Jet," *AIAA Journal*, Vol. 45, No. 7, 2007, p. 1675.
doi:10.2514/1.27497

[40] Singh, A., and Chatterjee, A., "Numerical Prediction of Supersonic Jet Screech Frequency," *Shock Waves*, Vol. 17, No. 4, 2007, pp. 263–272.
doi:10.1007/s00193-007-0110-1

[41] Deck, S., "Delayed Detached Eddy Simulation of the End-Effect Regime and Side-Loads in an Overexpanded Nozzle Flow," *Shock Waves*, Vol. 19, No. 3, 2009, pp. 239–249.
doi:10.1007/s00193-009-0199-5

[42] Powell, A., "The Sound-Producing Oscillations of Round Underexpanded Jets Impinging on Normal Plates," *Journal of the Acoustical Society of America*, Vol. 83, No. 2, 1988, pp. 515–533.
doi:10.1121/1.396146

[43] Courant, R., Isaacson, E., and Rees, M., "On the Solution of Non Linear Hyperbolic Differential Equations by Finite Differences," *Communications on Pure and Applied Mathematics*, Vol. 5, No. 3, 1952, pp. 243–255.
doi:10.1002/cpa.3160050303

[44] Donea, J., "A Taylor–Galerkin Method for Convective Transport Problems," *International Journal for Numerical Methods in Engineering*, Vol. 20, No. 1, 1984, pp. 101–119.
doi:10.1002/nme.1620200108

[45] Favre, A., *Problems of Hydrodynamics and Continuum Mechanics*, Society for Industrial and Applied Mechanics, Philadelphia, 1969.

[46] Pope, S. B., *Turbulent Flows*, Cambridge Univ. Press, Cambridge, England, 2000.

[47] Smagorinsky, J., "General Circulation Experiments with the Primitive Equations: 1. The Basic Experiment," *Monthly Weather Review*, Vol. 91, No. 3, 1963, pp. 99–164.
doi:10.1175/1520-0493(1963)091<0099:GCEWTP>2.3.CO;2

[48] Germano, M., "Turbulence: The Filtering Approach," *Journal of Fluid Mechanics*, Vol. 238, No. -1, 1992, pp. 325–336.
doi:10.1017/S0022112092001733

[49] Cook, A., and Cabot, W., "Hyperviscosity for Shock-Turbulence Interactions," *Journal of Computational Physics*, Vol. 203, No. 2, 2005, pp. 379–385.
doi:10.1016/j.jcp.2004.09.011

[50] Jameson, A., Schmidt, W., and Turkel, E., "Numerical Solution of the Euler Equations by Finite Volume Methods Using Runge–Kutta Time Stepping Schemes," AIAA 1981–1259, 1981.

[51] von Neumann, J., and Richtmeyer, R. D., "A Method for the Numerical Calculation of Hydrodynamic Shocks," *Journal of Applied Physics*, Vol. 21, No. 3, 1950, p. 232.
doi:10.1063/1.1699639

[52] Bogey, C., de Cacqueray, N., and Bailly, C., "A Shock-Capturing Methodology Based on Adaptative Spatial Filtering for High-Order Nonlinear Computations," *Journal of Computational Physics*, Vol. 228, No. 5, 2009, pp. 1447–1465.
doi:10.1016/j.jcp.2008.10.042

[53] Cook, A., and Cabot, W., "A High-Wavenumber Viscosity for High-Resolution Numerical Methods," *Journal of Computational Physics*, Vol. 195, No. 2, 2004, pp. 594–601.
doi:10.1016/j.jcp.2003.10.012

[54] Jiang, G. S., and Shu, C. W., "Efficient Implementation of Weighted ENO Schemes," *Journal of Computational Physics*, Vol. 126, No. 1, 1996, pp. 202–228.
doi:10.1006/jcph.1996.0130

[55] Cook, Andrew, W., and Cabot, William, H., "A High-Wavenumber Viscosity for High Resolution Numerical Methods," Lawrence Livermore Nat. Lab., Tech. Rept. UCRL-ID-152002Feb. 2003.

[56] Roux, A., Gicquel, L., Sommerer, Y., and Poinsot, T., "Large Eddy Simulation of Mean and Oscillating Flow in Side-Dump Ramjet Combustor," *Combustion and Flame*, Vol. 152, Nos. 1–2, 2008, pp. 154–176.
doi:10.1016/j.combustflame.2007.06.015

[57] Zapryagaev, V., Pickalov, V., Kiselev, N., and Nepomnyashchiy, A., "Combination Interaction of Taylor–Goertler Vortices in a Curved Shear Layer of a Supersonic Jet," *Theoretical and Computational Fluid Dynamics*, Vol. 18, No. 2, 2004, pp. 301–308.
doi:10.1007/s00162-004-0141-5

[58] Zapryagaev, V., Kiselev, N., and Pavlov, A., "Effect of Streamline Curvature on Intensity of Streamwise Vortices in the Mixing Layer of Supersonic Jets," *Journal of Applied Mechanics*, Vol. 45, No. 3, 2004, pp. 335–343.
doi:10.1023/B:JAMT.0000025014.73642.1d

[59] Krothapalli, A., Strykowski, P., and King, C., "Origin of Streamwise Vortices in Supersonic Jets," *AIAA Journal*, Vol. 36, No. 5, 1998, pp. 869–872.
doi:10.2514/2.450

[60] Hussain, F., and Jeong, J., "On the Identification of a Vortex," *Journal of Fluid Mechanics*, Vol. 285, No. -1, 1995, pp. 69–94.
doi:10.1017/S0022112095000462

[61] Pope, S. B., "Ten Questions Concerning the Large-Eddy Simulation of Turbulent Flows," *New Journal of Physics*, Vol. 6, 2004, p. 35.
doi:10.1088/1367-2630/6/1/035

[62] Senoner, J., Sanjosé, M., Lederlin, T., Jaegle, F., García, M., Riber, E., Cuenot, B., Gicquel, L., Pitsch, H., and Poinsot., T., "Evaluation of Numerical Strategies for Two-Phase Reacting Flows," *Comptes Rendus Hebdomadaires des Seances de l'Academie des Sciences*, Vol. 337, Nos. 6–7, 2009, pp. 528–538.

[63] Metais, O., and Lesieur, M., "Statistical Probability of Decaying Turbulence," *Journal of the Atmospheric Sciences*, Vol. 43, No. 9, 1986, pp. 857–870.

[64] Vreman, B., Geurts, B., and Kuerten, H., "Large-eddy simulation of the turbulent mixing layer," *Journal of Fluid Mechanics*, 1997.

[65] Celik, I., Cehreli, Z., and Yavuz, I., "Index of Resolution Quality for Large Eddy Simulations," *Journal of Fluids Engineering*, Vol. 127, No. 5, 2005, p. 949.
doi:10.1115/1.1990201

[66] Gant, S., "Reliability Issues of LES-Related Approaches in an Industrial Context," *Flow, Turbulence and Combustion*, Vol. 84, No. 2, 2010, pp. 325–335.
doi:10.1007/s10494-009-9237-8

[67] Sagaut, P., *Large Eddy Simulation for Incompressible Flows*, Springer, New York, 2002.

P. Givi
Associate Editor